MIT Open Access Articles

Modeling study of thermoelectric SiGe nanocomposites

Modeling study of thermoelectric SiGe nanocomposites

A. J. Minnich,[1] H. Lee,[1] X. W. Wang,[2] G. Joshi,[2] M. S. Dresselhaus,[3] Z. F. Ren,[2] G. Chen,[1,*] and D. Vashaee[4,†]

[1]*Department of Mechanical Engineering, Massachusetts Institute of Technology, Cambridge, Massachusetts 02139, USA*
[2]*Department of Physics, Boston College, Chestnut Hill, Massachusetts 02467, USA*
[3]*Department of Physics and Department of Electrical Engineering and Computer Science,*
Massachusetts Institute of Technology, Cambridge, Massachusetts 02139, USA
[4]*School of Electrical and Computer Engineering, Oklahoma State University, Tulsa, Oklahoma 74106, USA*

Nanocomposite thermoelectric materials have attracted much attention recently due to experimental demonstrations of improved thermoelectric properties over those of the corresponding bulk material. In order to better understand the reported data and to gain insight into transport in nanocomposites, we use the Boltzmann transport equation under the relaxation-time approximation to calculate the thermoelectric properties of *n*-type and *p*-type SiGe nanocomposites. We account for the strong grain-boundary scattering mechanism in nanocomposites using phonon and electron grain-boundary scattering models. The results from this analysis are in excellent agreement with recently reported measurements for the *n*-type nanocomposite but the experimental Seebeck coefficient for the *p*-type nanocomposite is approximately 25% higher than the model's prediction. The reason for this discrepancy is not clear at the present time and warrants further investigation. Using new mobility measurements and the model, we find that dopant precipitation is an important process in both *n*-type and *p*-type nanocomposites, in contrast to bulk SiGe, where dopant precipitation is most significant only in *n*-type materials. The model also shows that the potential barrier at the grain boundary required to explain the data is several times larger than the value estimated using the Poisson equation, indicating the presence of crystal defects in the material. This suggests that an improvement in mobility is possible by reducing the number of defects or reducing the number of trapping states at the grain boundaries.

I. INTRODUCTION

Thermoelectrics are of technological interest due to their ability to convert heat directly into electrical energy. They have been the subject of renewed research due to theoretical predictions[1–3] and experimental demonstrations of nanostructured materials with enhanced thermoelectric properties.[4–19]

The performance of these materials depends on the dimensionless figure of merit $ZT = S^2 \sigma T / \kappa$, where S is the Seebeck coefficient, σ is the electrical conductivity, κ is the thermal conductivity, and T is the absolute temperature at which the properties are measured.[20,21]

Nanocomposite thermoelectric materials, simply termed nanocomposites, are a type of nanostructured material which have attracted much attention recently due to experimental demonstrations of improved thermoelectric properties over those of the corresponding bulk material.[7,8,10,12,16–19] These materials have an important advantage over other nanostructured materials in that they can be produced in large quantities and in a form that is compatible with existing thermoelectric device configurations. The term "nanocomposite" has been used to describe several different types of structures. The original concept was applied to either nanoparticles embedded in a host or to a heterostructure geometry with nanoparticles of different materials adjacent to each other.[22,23] For the heterostructure geometry, when the two materials are the same, the nanocomposite is essentially a material with nanometer-sized grains. The physical mechanisms that can lead to *ZT* improvement in heterogeneous and nanograined materials are similar: in both cases, the grain boundaries act as an additional phonon-scattering mecha-

nism, reducing the lattice thermal conductivity; while a potential barrier, or an electron energy mismatch, at the grain boundary leads to a reduced electrical conductivity but possibly higher Seebeck coefficient. Nanocomposites are commonly created using either a ball milling and hot pressing technique[16–19] or with thermal processing methods.[7,8,10,12]

The thermoelectric properties of $Si_{0.8}Ge_{0.2}$ nanocomposites with improved properties over those of the bulk were recently reported.[18,19] To better understand the reported data and to gain insight into the carrier transport, we calculate the thermoelectric properties of these materials using the Boltzmann transport equation. The theory for modeling bulk thermoelectric materials using the Boltzmann transport equation is well developed and the calculation is straightforward. If the relaxation-time approximation can be used, the thermoelectric properties can be expressed as integrals of a relaxation time,[24–26] and standard expressions for the relaxation time of various scattering mechanisms are given in the literature.[25–27] For the cases that we study here the relaxation-time approach is a good approximation. A similar approach was taken by Vining[28] and Slack and Hussain,[29] and we follow their work closely with a few important exceptions which will be described later. To model transport in nanocomposites using this framework, we need to obtain an additional relaxation time τ_{GB} (or equivalently a scattering rate τ_{GB}^{-1}) to account for the strong grain-boundary (GB) scattering mechanism in these materials. Once determined, this scattering rate can be added to the other scattering rates using Matthiessen's rule and the thermoelectric properties are calculated in the usual manner.

Grain-boundary scattering has been of great interest, particularly for device applications involving polycrystalline

TABLE I. Band structure parameters for $Si_{1-x}Ge_x$ used to calculate electrical properties.

Property	Symbol (units)	Value	Comment
Electron longitudinal/transverse effective mass (X)	$m_l^*/m_t^*(m_e)$	0.92/0.19	Ref. 49
Electron longitudinal/transverse effective mass (L)	$m_l^*/m_t^*(m_e)$	1.59/0.082	Ref. 49
Energy gap between X and L	E_L (eV)	0.8	Ref. 49
Hole DOS effective mass (bulk/nano)	$m_h^*(m_e)$	1.2/1.55	Ref. 29
Nonparabolicity of X	α (eV^{-1})	1.25	Ref. 48: 0.5
Low-frequency dielectric constant	$\epsilon_{0r}(\epsilon_0)$	21	Ref. 49: 11.7+4.5x; Ref. 28: 27
Electron deformation potential	D_A (eV)	10.5	Ref. 48: 9.0
Hole-deformation potential	D_v (eV)	4.8	Ref. 28: 2.94; Ref. 26: 5.0

silicon. Mayadas and Shatzkes[30] obtained a scattering rate from a series of delta-function potentials. Their model is commonly used to calculate the resistivity of polycrystalline materials. We will show that this model is not physically consistent for thermoelectric materials. Many other models for grain-boundary scattering in polycrystalline materials attempt to obtain *I-V* characteristics by considering thermionic field-emission and tunneling processes.[31–34] However, this framework neglects the energy relaxation of charge carriers and can result in unrealistically large Seebeck coefficients, especially in nanocomposites. For this reason, we focus on calculating grain-boundary scattering rates, allowing all the properties to be determined in a self-consistent manner.

The organization of the paper is as follows. First, in Sec. II, the basic theory of calculating thermoelectric properties using the Boltzmann equation is briefly dicussed. In Sec. III, the code which implements this calculation is validated by calculating the thermoelectric properties of bulk $Si_{1-x}Ge_x$ alloys and comparing the results to experimental data. Section IV introduces models for phonon and electron grain-boundary scattering. We apply the models to $Si_{0.8}Ge_{0.2}$ nanocomposites in Sec. V and compare the results to recently reported experimental data[18,19] and new mobility measurements. Finally, in Sec. VI, we use the model's predictions to help determine which strategies will be most effective in further improving the figure of merit in these materials.

II. THEORY

The thermoelectric properties of $Si_{1-x}Ge_x$ can be calculated using the Boltzmann equation. If all the scattering mechanisms are elastic, the relaxation-time approximation (RTA) may be employed, simplifying the solution.[25–27,35] If some scattering mechanisms are inelastic, then a relaxation time cannot be strictly defined. For $Si_{1-x}Ge_x$, the only inelastic-scattering mechanism is due to optical phonons, where the interaction energy $\hbar\omega_{op}$, with ω_{op} being the optical-phonon frequency, is on the order of $k_B T$ at room temperature. Fortunately, for heavily doped $Si_{1-x}Ge_x$, most carriers have energies several times larger than the optical-phonon energies, making the assumption of elastic scattering a reasonable one and allowing the use of the RTA for our calculations.

A very similar approach to calculate the thermoelectric properties of bulk materials was originally performed by sev-

eral authors,[28,29] and we follow their work closely but with important exceptions. The common calculations are as follow. First, like Slack,[29] we assume three-band transport, using two conduction bands, one near the X point and one at the L point; and one effective valence band. We find that the L-point conduction band does not contribute substantially to the transport properties. Second, like Vining,[28] we take into account the exact form of the relaxation times from the literature.[25,26,28,36] Slack uses an effective relaxation-time exponent or empirical results in his model.

We differ from the others' calculations in the following ways. The first difference is that we do not assume that the conduction bands and valence bands have the same band-structure parameters; instead, we use literature or slightly modified values for each band. These values are listed in Table I.

The second difference is that we take into account the nonparabolicity of the X-point conduction band, which strongly affects the thermoelectric properties at high n-type doping concentrations.[26] Vining and Slack did not take nonparabolicity into account, and while they were able to fit most of the data, unphysical values of some fitting parameters were required, or an empirical result was used to obtain agreement. By using a nonparabolic formulation we are able to explain experimental data over the entire doping concentration range with only minor adjustments to the literature values of the band-structure parameters.

Another important difference is the treatment of dopant precipitation issues in $Si_{1-x}Ge_x$. As discussed by many authors,[28,29,37–39] $Si_{1-x}Ge_x$ alloys used for thermoelectrics, which are usually doped with P (n type) or B (p type), are often doped beyond the solubility point for the dopant, causing the carrier concentration to vary with temperature as dopants precipitate out at lower temperatures and become reactivated at higher temperature. These processes can change the carrier concentration by a factor of 2 or more over the entire temperature range, significantly affecting the observed transport properties. This effect is especially pronounced for P in $Si_{1-x}Ge_x$, which has a strong tendency to precipitate at grain boundaries. Furthermore, in many cases the carrier concentration depends on the thermal history of the sample, making it even more difficult to compare results because the properties of the same material at the same temperature might not be equal due to differences in thermal processing. While Vining was forced to fit the chemical potential at each

temperature to account for this variation, we are able to estimate the change in carrier concentration versus temperature during the electrical conductivity and Seebeck coefficient measurement using the previously reported electrical conductivity measurements,[18,19] new mobility measurements, and model calculations. This procedure simply uses the definition of conductivity $\sigma = ne\mu$ for a single band to estimate $n(T)$. It is necessary to assume one-band transport for this procedure; we find this to be a valid assumption for the cases studied here due to heavy doping. For the n-type case, where the mobility has a stronger dependence on the carrier concentration, an iterative procedure is used to ensure self-consistency between all the properties.

A final point to mention is the difficulty in accurately modeling transport in p-type $Si_{1-x}Ge_x$ using the Boltzmann equation. The warped energy surface of the heavy-hole band, along with interactions from the split-off band (which is only 0.044 eV away from the valence-band edge), causes the parabolic energy surface approximation to be poor at high doping levels. While it is sometimes possible to obtain a reasonable fit to the data, the quality of the fit is often worse than that of n-type $Si_{1-x}Ge_x$, and for the p-type nanocomposite no satisfactory fit could be found. The valence-band parameters used in the calculation are listed in Table I.

A. Relaxation-time approximation

Under the relaxation-time approximation, the electrical conductivity, Seebeck coefficient, mobility, and electronic thermal conductivity can be written as integrals of the form

$$L_k = \int \tau(E) v^2 \left(-\frac{\partial f_0}{\partial E} \right) (E - E_f)^k D(E) dE, \tag{1}$$

where E is the energy, $D(E)$ is the density of states, $f_o = \{\exp[(E - E_f)/k_B T] + 1\}^{-1}$ is the Fermi-Dirac distribution function, v is the electron group velocity, $\tau(E)$ is the relaxation time, and E_f is the Fermi level. Detailed expressions for the properties are given in many references[24–27] and will not be reproduced here. The Fermi level is determined from the standard charge conservation condition.[25–27]

To accurately model $Si_{1-x}Ge_x$, it is necessary to account for nonparabolicity and anisotropy. We use a standard two-band approximation,[26,27] which modifies the $E(k)$ dispersion relation from the usual parabolic form to

$$E(1 + \alpha E) = \frac{\hbar^2}{2} \left(\frac{k_l^2}{m_l^*} + 2\frac{k_t^2}{m_t^*} \right), \tag{2}$$

where m_l^* and m_t^* are the longitudinal and transverse components of the effective mass, respectively; k_l and k_t are the longitudinal and transverse components of the electron wavevector; and α is the nonparabolicity coefficient, an adjustable parameter which is approximately $\alpha \approx 1/E_g$, with E_g being the bandgap.[26] The temperature dependence of the band gap $E_g(T)$ is accounted for using a curve fit from Ref. 64. The density of states, electron velocity, and conductivity mass for this modified dispersion relation are given in several references.[26,27,40]

It is important to account for the effects of both electron and hole transport, especially at high temperature where bi-

polar thermal conduction can occur. Multiple-band transport can be incorporated by calculating the contribution from each band and combining the results in the appropriate manner, given in Ref. 20.

B. Charge-carrier relaxation times

The relaxation times account for the scattering processes in a material. In this paper we will be modeling $Si_{0.8}Ge_{0.2}$ and will incorporate ionized impurity scattering (IIS) and phonon deformation-potential (DP) scattering. Note that $Si_{1-x}Ge_x$ is not a polar material and thus polar scattering mechanisms are not applicable. Technically $Si_{1-x}Ge_x$ also has an alloy scattering mechanism but the scattering rate due to alloy scattering has the same energy dependence as that of phonon scattering and so is accounted for with an effective deformation potential. The relaxation times used here incorporate nonparabolicity. Various forms of the relaxation times are in the literature and give similar results.[25–27,35,36,41]

The first scattering mechanism, ionized impurity scattering, has a relaxation time given by the standard Brooks-Herring result.[25,26] For highly doped materials, it is more appropriate to use the Thomas-Fermi approximation for the screening length, which is given by[40,42]

$$R^{-2} = \frac{4\pi e^2 Z}{\varepsilon_\infty} \int_0^\infty \left(-\frac{\partial f_0}{\partial E} \right) D(E) dE, \tag{3}$$

where e is the absolute value of the charge of an electron, Z is the number of charges per impurity and ε_∞ is the high frequency permittivity.

Phonon scattering in SiGe requires more discussion. In general, charge carriers can be scattered by both acoustic and optical phonons. When the carriers have energy greater than the optical-phonon energy, the optical-phonon scattering rate is usually dominant. In pure silicon, intravalley optical-phonon scattering in the X valley is forbidden due to selection rules but intervalley scattering between the six X valleys of equivalent energy can take place through nonpolar optical-phonon (NPOP) scattering. The scattering rate for intervalley scattering is usually calculated using a deformation-potential-type analysis[26] and values of the optical-phonon energies and coupling constants have been inferred from experiment and Monte Carlo simulations.[43–46]

However, the materials we examine in this study are quite different from single-crystal silicon or germanium, and we find that the intervalley parameters inferred for silicon, germanium, or an interpolation of the two, cannot explain the experimental data we analyze in this work. The most likely reasons for this discrepancy are the different phonon spectra between single-crystal silicon or germanium and SiGe alloys, and different coupling constants due to additional scattering mechanisms and high carrier concentrations in the SiGe alloys.[47]

As there are no experimental data available on the optical-phonon modes in bulk or nanocomposite SiGe, to proceed, it is necessary to perform some type of fit to explain the data. As the scattering rates due to acoustic-phonon scattering and intervalley scattering have the same energy dependence, fitting an effective deformation potential and fitting a coupling

constant and optical-phonon energy should give equivalent results. Using our model, we have verified that the mobilities calculated from these scattering rates have essentially the same slope with temperature, as expected. Hence, we can account for both acoustic-phonon and intervalley scattering using an effective deformation potential. This type of approximation is discussed in Ref. 36, and Vining also used a single deformation potential in his study.[28]

It should be noted that the relaxation-time approximation is not strictly valid for the inelastic NPOP mechanism and if carrier energies are comparable to the optical-phonon energy the approximation will fail. In the highly doped materials studied here, however, the Fermi level is up to 0.2 eV in the conduction or valence bands, and hence most carriers have energies greater than the typical optical-phonon energy of 20–50 meV, making the assumption of elastic scattering a reasonable approximation.

The relaxation time τ_{DP} for phonon deformation-potential scattering is taken from Ravich,[36]

$$\tau_0^{-1} = \frac{\pi k_B T D_A^2}{\rho v_s^2 \hbar} D(E),\qquad(4)$$

$$\tau_{DP}^{-1} = \bar{\tau}_0^{-1}\left\{\left[1 - \frac{\alpha E}{1+2\alpha E}\left(1 - \frac{D_v}{D_A}\right)\right]^2 - \frac{8}{3}\frac{\alpha E(1+\alpha E)}{(1+2\alpha E)^2}\frac{D_v}{D_A}\right\},\qquad(5)$$

where E is the energy relative to the band edge, D_A is the conduction-band deformation potential, D_v is the valence-band deformation potential, α is the nonparabolicity parameter, $D(E)$ is the density of states, ρ is the density, and v_s is the sound speed. The values of the electron and hole deformational potentials used are listed in Table I.

To obtain a total relaxation time for all the scattering mechanisms, we can add the scattering rates τ^{-1} using Matthiessen's rule $\tau^{-1} = \Sigma_i \tau_i^{-1}$.[25,26]

C. Phonon modeling

To model phonon transport, we use the Steigmeier and Abeles model[47] of the lattice thermal conductivity of alloys based on the Callaway model.[50] Their model treats phonons with the Boltzmann equation under the RTA and includes point-defect, phonon-phonon, and phonon-electron-scattering mechanisms, all of which are characterized by a relaxation time.[47] These relaxation times are used exactly as they are given in Ref. 47 and so are not reproduced here. One important point is that the deformation potentials used in the phonon-electron relaxation times are not the same as those used in the electronic properties calculation. The reason is that the primary contribution to the thermal conductivity is from acoustic phonons but the deformation potentials used for the electronic properties calculations account for both acoustic and optical phonons. Thus, we use slightly smaller deformation potentials for the thermal-conductivity calculation which are consistent with the values given in Ref. 47.

Once the relaxation times have been computed, the lattice thermal conductivity κ_l can be determined

$$\kappa_l = \frac{k_B}{2\pi^2 v_s}\left(\frac{k_B \theta_D}{\hbar}\right)^3 (I_1 + I_2^2/I_3),\qquad(6)$$

where v_s is the sound speed, θ_D is the Debye temperature, and I_1, I_2, and I_3 are given by

$$I_1 = \int_0^1 \tau x^2 \frac{\nu^2 x^2 e^{\nu x}}{[\exp(\nu x) - 1]^2}dx,\qquad(7)$$

$$I_2 = \beta \int_0^1 \frac{\tau}{\tau_U} x^2 \frac{\nu^2 x^2 e^{\nu x}}{[\exp(\nu x) - 1]^2}dx,\qquad(8)$$

$$I_3 = \beta \int_0^1 \frac{1}{\tau_U}\left(1 - \frac{\beta\tau}{\tau_U}\right)x^2 \frac{\nu^2 x^2 e^{\nu x}}{[\exp(\nu x) - 1]^2}dx.\qquad(9)$$

Here $x = \omega/\omega_D$, where ω_D is the Debye frequency, $\nu = (\theta_D/T)^n$, $n \approx 1$ is a fitting parameter related to higher-order phonon scattering, β is the ratio of Umklapp to normal-mode scattering, and τ and τ_U are the total and Umklapp relaxation times, respectively. The total thermal conductivity κ is the sum of the lattice thermal conductivity κ_l and the electronic thermal conductivity κ_e.

D. Summary of the calculation

We now review the steps necessary to perform the calculation. After specifying band-structure parameters, temperature, and doping level, the first step is to calculate the Fermi level. The next step is to compute the energy-dependent relaxation times and combine them using Matthiessen's rule. Once the total relaxation times are determined, we can compute the thermoelectric properties for each band, and subsequently calculate the overall transport properties. Finally, the lattice thermal conductivity can be calculated separately using the Callaway model.[47,50] This procedure can be repeated for each temperature or doping concentration, allowing all of the thermoelectric properties to be determined over the desired temperature and doping concentration ranges.

III. MODEL VALIDATION

To validate the model, we compare the calculated results to experimental data for bulk $Si_{1-x}Ge_x$ from several sources.[18,19,28,51] The parameters used are listed in Tables I and II.

The modeling predictions for bulk *n*-type $Si_{0.7}Ge_{0.3}$, along with the same data used by Vining for comparison,[28,51] are shown in Fig. 1. The calculations match the experimental data to within about 15% over most of the doping concentration and temperature range. The two highest doping concentrations have been increased by about 10% from the reported values; this adjustment is expected to be within the experimental error of the measurement. Some of the important effects discussed earlier can be clearly seen in the model; for example, for the lowest doping concentration the bipolar thermal conductivity is dominant at high temperatures, and is accompanied by a large decrease in Seebeck coefficient. The most highly doped material shows evidence

TABLE II. Lattice parameters for $Si_{1-x}Ge_x$ used to calculate the lattice thermal conductivity.

Property	Symbol (units)	Value	Comment
Lattice constant	a (Å)	$5.431(1-x)+5.658x$	Ref. 49
Bulk modulus	$C_1(10^{10}$ N/m$^2)$	$9.8-2.3x$	Ref. 49
Debye temperature	Θ_D (K)	$640-266x$	Ref. 49
Density	ρ (kg/m^3)	$2329+3493x-499x^2$	Ref. 49
Ratio of normal to Umklapp scattering	β	2.0	Ref. 47
Anharmonicity (n type)	γ_l	0.9	Ref. 47
Anharmonicity (p type)	γ_l	0.75	
Strain parameter	ϵ_s	100	Ref. 47
Electron-acoustic deformation potential	E_{cl} (eV)	9.0	Ref. 47
Hole-acoustic deformation potential	E_{vl} (eV)	4.0	Ref. 47
Higher-order phonon-scattering exponent	n	1.4	

of dopant activation above 1000 K, seen as an increase in the electrical conductivity, but this is not accounted for here as the mobility is unknown.

A similar result for p-type $Si_{0.7}Ge_{0.3}$, along with data from Dismukes,[51] is shown in Fig. 2. The fit is slightly worse than that for the n-type case, particularly for the Seebeck coefficient, as this parameter is sensitive to the band structure and is most affected by the failure of the parabolic approximation. At high temperature the Seebeck coefficient is underestimated by about 20% in the worst case. The room-temperature thermal conductivities are also lower than the experimental values, illustrating the difficulty in fitting many data sets with only one set of parameters. As discussed in Ref. 47, the acoustic deformation potential appears to be a function of carrier concentration, but we have used a single acoustic deformation potential for simplicity. The × symbols in the figure indicate that the accuracy of some of the experimental data is questionable as the maximum ZT value for the highest two doping concentrations is almost $ZT=0.8$, higher than the expected value of around 0.5–0.6 for state-of-the-art bulk $Si_{0.8}Ge_{0.2}$ shown in Fig. 4.

We also computed the thermoelectric properties of state-of-the-art n-type and p-type $Si_{0.8}Ge_{0.2}$ alloys,[18,19] shown in Figs. 3 and 4. In this case the carrier concentrations are not available, forcing us to adjust the values to fit the data. The fitted carrier concentrations were determined to be $N_D=1.7 \times 10^{20}$ cm^{-3} for n type and $N_A=1.35\times 10^{20}$ cm^{-3} for p type. The calculation is again in good agreement with the experimental data over the temperature range. As expected, the n-type material exhibits a strong carrier-concentration variation with temperature due to dopant precipitation effects. To account for this, the calculated mobility and the experimental electrical conductivity are used to estimate the carrier-concentration variation with temperature using $\sigma=ne\mu$. As the mobility depends on the carrier concentration to some extent, an iterative procedure is employed to ensure consistency between all the properties. The carrier-concentration variation is found to be similar to that deduced for the n-type nanocomposite, and using either curve will give a good fit;
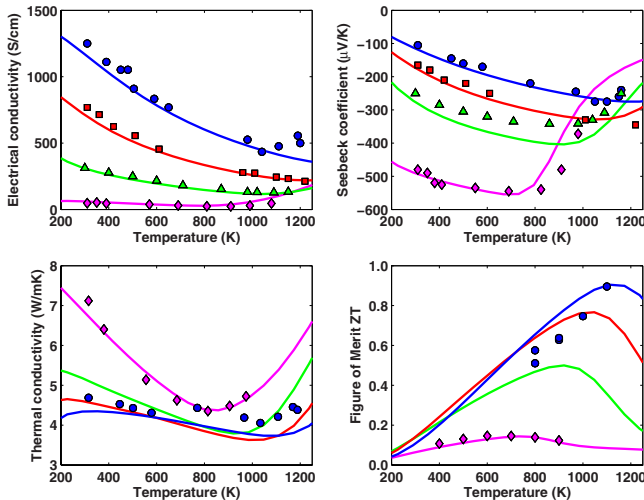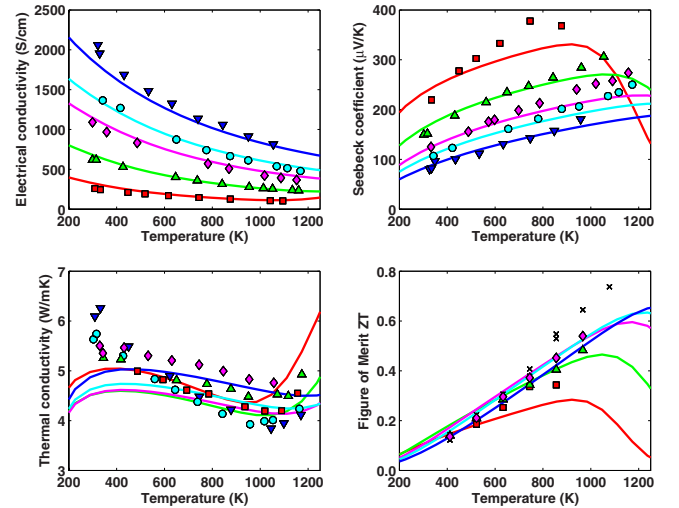

FIG. 1. (Color online) Experimental (symbols) and computed (curves) thermoelectric properties of n-type bulk $Si_{0.7}Ge_{0.3}$ (data from Ref. 28). Doping concentrations ($\times 10^{19}$ cm^{-3}): $\diamond$ =0.22; $\triangle$ =2.3; $\square$ =7.3; and $\bigcirc$ =17.

FIG. 2. (Color online) Experimental (symbols) and computed (curves) thermoelectric properties of p-type bulk $Si_{0.7}Ge_{0.3}$ (data from Ref. 51). Doping concentration ($\times 10^{19}$ cm^{-3}): $\square$ =3.4; $\triangle$ =8.9; $\diamond$ =18; $\bigcirc$ =24; and $\triangledown$ =35. × symbols in the ZT figure indicate the accuracy of the data is questionable as the ZT value is much higher than previously reported values for bulk p-type $Si_{1-x}Ge_x$.
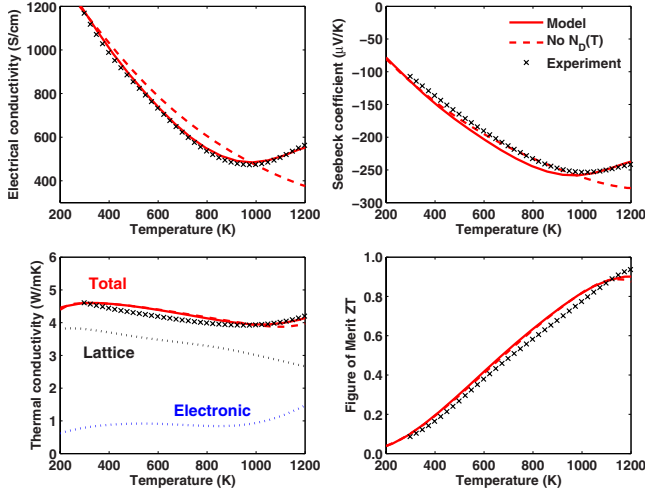
FIG. 3. (Color online) Experimental (symbols) and calculated (curves) thermoelectric properties of state-of-the-art *n*-type bulk $Si_{0.8}Ge_{0.2}$. (Solid line—model including carrier-concentration variation with temperature; dashed line—model without carrier-concentration variation with temperature; dotted lines—electronic and lattice components of thermal conductivity.)

the fit using the bulk experimental data is used for both cases as it gives smoother results.

IV. MODELING NANOCOMPOSITES

$Si_{1-x}Ge_x$ nanocomposites can have markedly different transport properties from their bulk counterparts. Grain boundaries in materials can act as interfaces to scatter phonons,[2] electrical traps for charge carriers,[52–54] and segregation sites for dopant atoms.[28,54] In nanocomposites these effects are further enhanced because the grain size is often comparable to or smaller than characteristic lengths such as the phonon mean-free path (MFP) or the electron wave-
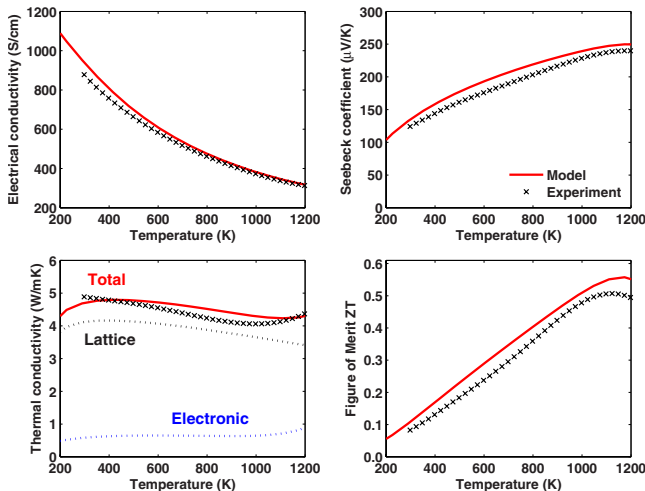

FIG. 4. (Color online) Experimental (symbols) and calculated (curve) thermoelectric properties of state-of-the-art *p*-type bulk $Si_{0.8}Ge_{0.2}$. (Solid line—model; dotted lines—electronic and lattice components of thermal conductivity.)

length. TEM images also show that the microstructure of nanocomposites is much more complicated than that of microcrystalline materials; in nanocomposites the nanometer-sized grains contain defects and composition variations, and the nanometer-sized grains themselves are embedded inside larger grains.[17–19] We focus our discussion on the effects of grain boundaries between the nanometer-sized grains as these are expected to have the largest impact on transport properties.

The most obvious way the thermoelectric properties are affected by grain boundaries is by a reduction in lattice thermal conductivity, which is the dominant mechanism of *ZT* enhancement in $Si_{1-x}Ge_x$ nanocomposites.[18,19] It is also found that the presence of grain boundaries reduces the electrical conductivity and can affect the Seebeck coefficient. The physical mechanisms for these changes in the transport properties of polycrystalline materials have been the subject of much discussion, especially for polycrystalline silicon.[31,32] The reduction in the lattice thermal conductivity is attributed to strong interface scattering of phonons.[2] For charge carriers, the generally accepted model to explain the effects of grain boundaries is the charge-trapping model.[52–54] This model postulates that incomplete bonding in grain boundaries leads to the formation of many surface states within the band gap, making it preferable for carriers to occupy these lower-energy states. Due to a depletion of the grain near the grain boundary, a space-charge region with a potential barrier forms; this potential acts as a scattering potential for charge carriers. Dopant segregation is also thought to affect the electrical properties of grain boundaries, though if and how the grain boundaries are affected is not well understood.[54] Misalignment of crystallographic directions between adjacent grains can also lead to electron-scattering processes.[55]

To obtain quantitative predictions of how grain boundaries affect the thermoelectric properties in nanocomposites using the Boltzmann equation, it is necessary to develop phonon and charge-carrier grain-boundary scattering models which give a grain-boundary scattering rate τ_{GB}^{-1}. The resulting scattering rates can then be added to the bulk scattering rate and the thermoelectric properties calculated in the usual manner. We now develop the grain-boundary scattering models. Here, we specialize the situation for charge-carrier scattering to electrons in an *n*-type material; the same discussion will apply to holes in a *p*-type material.

A. Phonon scattering

There have been several previous efforts to determine the thermal conductivity of nanocomposites. Yang *et al.*[22,23] calculated the effective thermal conductivity of a nanocomposite using the phonon Boltzmann equation. Monte Carlo techniques have also been used to calculate the thermal conductivity, giving good results but requiring significant computational time.[56] Prasher[57,58] has had considerable success obtaining analytical solutions to the Boltzmann equation for simple geometries. Scattering models based on Rayleigh scattering[59] and acoustic Mie scattering theory[60] have also been used to treat nanoparticle scattering. Minnich and

Chen[61] introduced a modified theory to analytically compute the thermal conductivity of nanocomposites.

For the present work we use a standard boundary scattering rate.[14,59] We can derive the model by examining characteristic lengths relevant to phonon transport. In this case the appropriate lengths are the phonon mean-free path relative to the grain size. Our calculations for bulk $Si_{0.8}Ge_{0.2}$ indicate that a large fraction of phonons have a MFP L_{PH} of about 100 nm, which is much larger than the nanocomposite grain size l_{gb} of about 10–20 nm. A reasonable model is thus one which approximates the phonon MFP in nanocomposites to be limited to the grain size such that $L_{PH}=l_{gb}$. Then, using the sound speed as the phonon velocity, as in the Debye model, the scattering rate follows immediately,

$$\tau_{\mathrm{GB}}^{-1} = \frac{v_s}{l_{gb}}. \tag{10}$$

This is added to the other phonon-scattering rates and the lattice thermal conductivity calculated in the same manner. We are able to obtain a good fit to the thermal-conductivity data using a grain size l_{gb} of 10–20 nm, which is consistent with the experimental values recently reported.[18,19]

B. Electron scattering

The grain-boundary model for electrons is based on the charge-trapping model, which postulates that the formation of surface states at the grain boundary depletes the grain of carriers near the grain boundary, resulting in a space-charge region with a potential barrier. The potential barrier acts as a scattering potential which affects electron transport. To calculate electrical properties, it is necessary to develop a model which can describe this phenomenon with a relaxation time. But to create a consistent model it is necessary to clarify details of the GB scattering process. Important questions that must be answered are what is a physical value for the GB potential, whether the electron wave experiences diffuse or coherent scattering, and over what length scale the grain-boundary potential affects the electrons.

The first question, an appropriate value for the GB potential, can be answered using a depletion region approximation. This analysis yields the following equation for the GB potential, assuming all the trap states are filled[52]

$$U_g = \frac{eN_t^2}{8\epsilon N_D}, \tag{11}$$

where ϵ is the permittivity, N_D is the doping concentration, and N_t is the number density of traps. Given the doping level N_D and trap density N_t, U_g can be estimated. Of course, the trap density is unknown and could vary widely. An important unresolved question is how dopant segregation affects the distribution and quantity of surface states.[54] It is known that P in $Si_{1-x}Ge_x$ has a strong tendency to precipitate to the GB,[28] and, in principle, the extra dopant atoms in the GB could affect the surface-state distribution. Assuming that the reported values for $N_t \approx 1 \times 10^{11} - 1 \times 10^{13}$ cm^{-3} are a reasonable estimate for our materials, at high doping levels this model predicts that U_g should be less than 20 meV.[54] How-

ever, we find that a larger GB potential is required to fit the nanocomposite data; we will discuss possible reasons for this discrepancy in Sec. VI.

The last two questions can be answered by examining the key length scales related to carrier transport in nanocomposites as was done for phonons. TEM and x-ray diffraction (XRD) measurements indicate that the average GB size is 10–20 nm and its thickness is around 1 nm.[18,19] We can determine how these length scales compare to carrier length scales by computing the screening length R, the electron wavelength λ_e, and the electron MFP.

The screening length R was previously given in Eq. (3). Computing this value shows that R is less than 1 nm, implying that the GB potential is completely screened unless the electron is within a few nanometers of the GB. Hence, we can conclude that the model should focus on only a small section of the GB since long-range potentials from other sections of the GB are neutralized by screening effects. The Mayadas model is not consistent with this result as it models the potential as a series of grain boundaries.

Next, the type of scattering must be determined. For example, if there are substantial variations in the potential at the GB we might expect the electron wave to be scattered diffusely, but if the variations are small, the scattering should be coherent. In addition, if the MFP is comparable to the grain size we might also expect multiple-scattering effects to be important. These questions can be resolved by calculating the distribution of electron wavelengths and MFPs. We first determine the cumulative distribution function of the electron occupation number versus wavelength, which gives the percentage of electrons that have a wavelength less than a certain value. The wavelength is given by the de Broglie expression,

$$\lambda_e = \frac{2\pi\hbar}{m_c^* v} = \frac{2\pi\hbar(1+2\alpha E)}{\sqrt{2m_c^* E(1+\alpha E)}}, \tag{12}$$

where v is the electron velocity and m_c^* is the conductivity effective mass. We define the transport electron occupation number as,

$$g_t = v^2\left(-\frac{\partial f_0}{\partial E}\right)D(E). \tag{13}$$

Integrating g_t to a certain value and normalizing the result will give the cumulative distribution function for the transport electron occupation number. Additionally, we can determine the electron MFP length using an equation of the form $l=v\tau$, where τ is the total bulk electron relaxation time. The electron MFP will in general be energy dependent, and we can relate the electron MFP to the wavelength λ_e by expressing each as a function of energy.

These two quantities, the transport electron wavelength cumulative distribution function and the electron MFP versus wavelength, are shown in Fig. 5 at 300 K for heavily doped bulk $Si_{0.8}Ge_{0.2}$. The first observation we can make is that most electrons have mean-free paths between 2 and 5 nm, which is smaller than the grain size. This fact implies that each small section of the grain with which the electron interacts is independent of the others: since the grain size is on
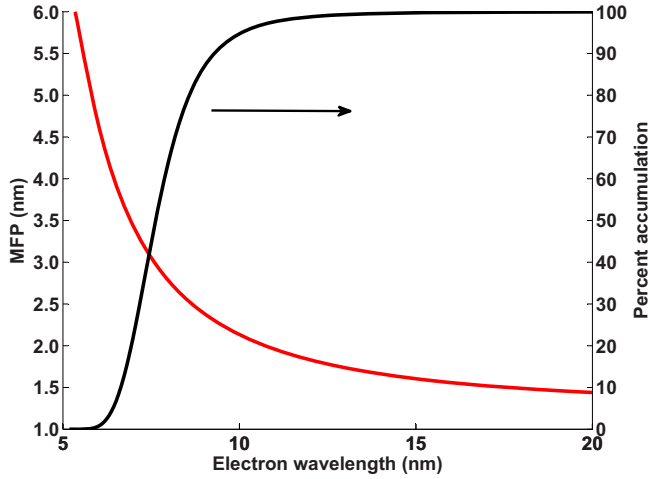
FIG. 5. (Color online) Computed results for the electron mean-free path versus electron wavelength (left axis), and percent accumulation of electron occupation number versus electron wavelength (right axis) for *n*-type ($N_D \approx 2 \times 10^{20}$ cm^{-3}) bulk Si$_{0.8}$Ge$_{0.2}$ at 300 K.

average on the order of 10–20 nm, after the electron scatters from the GB it will, on average, experience several collisions before it reaches another part of the GB. Thus the memory of the previous collision is essentially lost by the time the carrier reaches another part of the grain and we can conclude that each scattering point on the GB is independent from the others. This is further evidence against using the Mayadas model for thermoelectrics as it accounts for the effects of many grain boundaries scattering coherently.

The second observation is that most electrons have a wavelength between 6 and 11 nm, which is much larger than the GB thickness of 1 nm. Diffuse scattering of the electron wave requires substantial potential variation so that the wave is scattered randomly in all directions. Since the barrier potential is confined to a region very close to the GB itself, any spatial variation in the potential can only occur over a length on the order of the GB thickness. Furthermore, having a large variation in the value of the potential along the GB would require substantial nonuniformities which have not been observed in microstructure studies. These two results suggest that any variation in potential is not large and is confined to a region much smaller than the electron wavelength, which implies that the large variation in potential required for diffuse electron scattering is not present. Thus we can conclude that electrons for the most part should scatter coherently from the GB, enabling the use of scattering theory to calculate scattering rates of an electron wave from a scattering potential.

The third observation we make is that the electron MFP is predicted to be smaller than the wavelength, implying that the Boltzmann equation is at the edge of its validity. As the Boltzmann equation still gives good results for both the bulk and nanocomposite materials, the above discussion is still expected to hold. This issue is further discussed in Sec. VI.

Based on the above discussion, the physical picture for GB scattering is that of a carrier interacting with local regions of the GB with each region acting as an independent
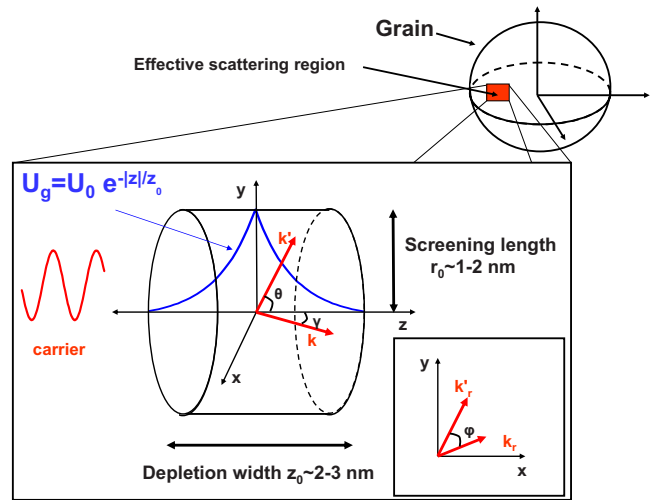
scattering site which coherently scatters an electron wave. The GB is composed of many of these scattering sites. The most appropriate model for GB scattering is therefore one which models only a local potential along a small section of the GB.

Using these results, we can now create an electron GB scattering model by identifying a scattering potential and calculating the corresponding scattering rate. We have developed a model which describes a small section of the grain boundary with a scattering potential U_g in a cylindrical region, as illustrated in Fig. 6. Since the actual GB is an extended planar defect, the modeled GB is composed of many such cylinders, each of which acts as an independent scattering site. The potential takes into account the variation in the potential along the direction perpendicular to the grain boundary. If r_0 is the radius of the cylinder, z is the direction normal to the GB, and $z=0$ is at the center of the GB, then the model potential is given by

$$U_g = \begin{cases} U_0 e^{-|z|/z_0} & r < r_0 \\ 0 & r > r_0 \end{cases} . \qquad (14)$$

Here U_0 is the maximum grain-boundary potential, r_0 is a constant on the order of the screening length R, and z_0 is a constant related to the size of the depletion region. This particular form of the potential is chosen for several reasons. The decaying exponential form of the potential in z is used as an approximation to the exact potential which would result from a carrier depletion region. The cylindrical geometry is chosen to model the effects of screening: within the cylinder the GB potential acts on the electron but beyond several multiples of the screening length the GB potential is screened out and is essentially zero.

With the scattering potential determined, the final step is to determine the scattering rate. We use the first Born approximation to calculate the scattering rate as the GB potential is not expected to be large. The matrix element for the potential is

FIG. 6. (Color online) Schematic of the cylinder model for electrical grain-boundary scattering.

$$M_{kk'} = \int e^{i\vec{k}\cdot\vec{r}} U_g(\vec{r}) e^{-i\vec{k}'\cdot\vec{r}} d^3r = \int e^{i\vec{q}\cdot\vec{r}} U_g(\vec{r}) d^3r \quad (15)$$

$$= 4\pi U_0 \left[\frac{z_0}{1+(q_z z_0)^2} \right] r_0^2 \left[\frac{J_1(q_r r_0)}{q_r r_0} \right], \quad (16)$$

where $J_1(q_r r_0)$ is a first-order Bessel function of the first kind, $\vec{q} = \vec{k} - \vec{k}'$, and q_r and q_z are the r and z components of $\vec{q}$, respectively. Here the r-z coordinate system is relative to that of the disk. From Fig. 6, we can express q_r and q_z in terms of γ, the angle between the z axis and $\vec{k}$; θ, the angle between the z axis and $\vec{k}'$; and ϕ, the angle between k_r and k_r'. The result is

$$q_z = k_z - k_z' = k(\cos \gamma - \cos \theta), \quad (17)$$

$$q_r = k\sqrt{\sin^2 \gamma + \sin^2 \theta - 2 \sin \gamma \sin \theta \cos \phi}. \quad (18)$$

The scattering rate and momentum relaxation times can be obtained from the expressions

$$S(k,k') = \frac{2\pi}{\hbar} |M_{kk'}|^2 \delta(E_{k'} - E_k), \quad (19)$$

$$\tau^{-1} = \frac{2}{(2\pi)^3} \int_0^{2\pi} \int_0^{\pi} \int_0^{\infty} S(k,k')(1-\cos\theta)k'^2 \sin\theta dk' d\theta d\phi. \quad (20)$$

Since the potential does not have spherical symmetry, evaluating the momentum relaxation time is more complicated and an analytic solution is not possible. Using the definitions above, the momentum relaxation time can be shown to be

$$\tau_{GB}^{-1} = \frac{8\pi^2 U_0^2 z_0^2 r_0^4 D(E)}{\hbar} N_g I(r_0, z_0), \quad (21)$$

$$I(r_0, z_0) = \frac{1}{\pi} \int_0^{2\pi} \int_0^{\pi} \int_0^{\pi} \frac{\sin\theta(1-\cos\gamma\cos\theta-\sin\gamma\sin\theta\cos\phi)}{[1+(q_z z_0)^2]^2} \frac{J_1^2(q_r r_0)}{(q_r r_0)^2} d\gamma d\theta d\phi, \quad (22)$$

where N_g is the number of cylinders per unit volume. An average has been performed over the incoming angles γ.

This scattering rate has two distinct regimes. For $q_z z_0 \ll 1$ (low-energy electrons), $\tau_{GB}^{-1} \propto E^{1/2}$, similar to the energy dependence of a diffusive boundary scattering rate. For $q_z z_0 \gg 1$ (high-energy electrons), $\tau_{GB}^{-1} \propto E^{-3/2}$, similar to the energy dependence of the ionized impurity-scattering rate. Depending on the value of the cylinder radius r_0, this change in energy dependence could give an energy filtering effect.

The final quantity needed is the density of cylinders N_g. If the grain boundary is modeled as a sphere, the number of cylinders per grain is simply the surface area of the sphere divided by the base area of the cylinder. The number density of cylinders is then just the number of cylinders per grain multiplied by the number density of grains,

$$N_g = \frac{1}{2} \frac{4\pi(l_{gb}/2)^2}{(\pi r_0^2)} \times \frac{1}{(l_{gb}/2)^3} \times f = \frac{4f}{l_{gb} r_0^2}. \quad (23)$$

The factor of 1/2 is necessary as each cylinder is shared between two grains. The parameter $0 < f < 1$ is a constant which accounts for the geometrical distribution of the cylinders. In the actual material, the cylinders are arranged according to the shape of the grain boundaries but in the derivation above it is implicitly assumed that the cylinders are uniformly distributed throughout the material. This could lead to an overestimation of the scattering rate. To estimate the magnitude of this effect, we implemented a simple Monte Carlo simulation which models a particle traveling through a three-dimensional lattice containing GB scattering sites in various geometries. In the first case, the GB sites are ar-

ranged along the faces of a cube, an approximation to their actual locations in the material; in the second case, the same number of GB sites are distributed uniformly throughout the region. After the particle passes through the GB site it is assumed the particle experiences an elastic, velocity-randomizing collision; the particle also experiences the same type of collision over a randomly chosen distance between 2 and 5 nm to account for other scattering processes. For each geometry, the number of times the particle passes through a GB site is recorded. This analysis indicates that assuming the same number of GB sites are uniformly distributed overestimates the number of times the particle is scattered by a GB site by approximately 30%. To compensate for this, we simply set $f \approx 0.7-0.8$ to reduce the effective density of cylinders. This is valid as it was previously shown that all the GB scattering sites should be independent of each other. The results are not particularly sensitive to the value of f: using a value of $f \pm 0.1$ will give a GB potential of approximately $U_g \pm 5$ meV. We use $f = 0.7$ for the calculations in this study.

With the scattering rate determined, the thermoelectric properties of nanocomposites can be determined by adding the GB scattering rate to the other scattering rates using Matthiessen's rule. To explain the nanocomposite data, suitable values of the model parameters will need to be determined. The adjustable parameters of the model are the barrier height U_g, the radius of the disk r_0, and the potential decay constant z_0. However, the parameters are not totally arbitrary: to be consistent with the characteristic lengths discussed before, r_0 must be on the order of the screening length, about 1–2 nm, and z_0 must be on the order of the space-charge region width, about 2–4 nm. The charge-trapping model predicts that U_g
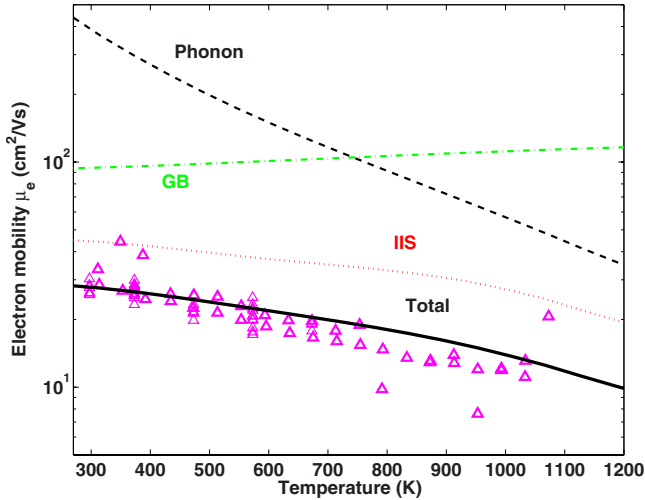
FIG. 7. (Color online) Calculated mobility for each scattering mechanism (phonon, GB, IIS) and total mobility (curves) with experimental data (symbols) for the *n*-type nanocomposite. (Solid line—total mobility; broken lines—mobility for each scattering mechanism.)

should be less than 20 meV, though the required GB potential turns out to be larger. In addition, for the lattice thermal-conductivity model the grain size must be specified; this is determined from XRD measurements to be on the order of 10–20 nm.[18,19]

V. RESULTS

Using these values as a guide, we have calculated the thermoelectric properties for *n*-type and *p*-type $Si_{0.8}Ge_{0.2}$ nanocomposites whose properties were recently reported.[18,19] The fitting procedure is as follows. First, with all other parameters kept constant, the parameters r_0, z_0, and U_g are adjusted so that the calculated mobility agrees with the experimental results. Next, the carrier concentration versus temperature variation is determined using the calculated mobility and the reported electrical conductivity. Finally, the electrical conductivity, Seebeck coefficient, thermal conductivity, and *ZT* are calculated. If the calculation is consistent, after fitting the mobility and carrier concentration the calculated results for all the properties should match the experimental data.

A. *n* type

We are able to obtain excellent agreement with the experimental data for the *n*-type nanocomposite using this procedure, indicating that the Boltzmann equation and the GB scattering model provide a good description of the transport. The calculated and experimental mobilities are shown in Fig. 7. IIS is the dominant scattering mechanism over most of the temperature range with GB scattering next most dominant at room temperature and acoustic-phonon scattering next most dominant above 700 K. The GB scattering fitting parameters used to obtain this result are summarized in Table III.

TABLE III. Fitting parameters used for nanocomposite modeling.

Material	U_g (meV)	r_0 (nm)	z_0 (nm)	l_{gb} (nm)
n-type $Si_{0.8}Ge_{0.2}$	45	1.0	2.0	12
p-type $Si_{0.8}Ge_{0.2}$	45	1.0	2.0	20

Figure 8 shows the *n*-type and *p*-type carrier concentrations versus temperature. For the *n*-type nanocomposite, there is a slight decrease in electron concentration with temperature at intermediate temperature, followed by a large increase in electron concentration with temperature at elevated temperature. This behavior is consistent with previous reports, as dopant precipitation to the GB in *n*-type $Si_{1-x}Ge_x$ is known to be a significant process even at intermediate temperatures of 600–700 K.[28,39] At room temperature the material is a supersaturated solution of $Si_{0.8}Ge_{0.2}$ and P as it has been quenched in air to room temperature, freezing the dopants in place. As the temperature is increased P is rejected from the lattice as the material attempts to return to its equilibrium state. At high temperature, the dopants are reactivated due to the increasing solubility limit and the electron concentration increases. Somewhat unexpectedly, the presence of additional grain boundaries in the nanocomposite does not seem to exacerbate this phenomenon; the bulk and nanocomposite materials exhibit very similar carrier concentration versus temperature curves.

The calculated thermoelectric properties, including dopant precipitation effects, are shown in Fig. 9, along with the nanocomposite experimental data and the calculated results without GB scattering for comparison. The calculated results which include GB scattering are in excellent agreement with the experimental results. Dopant precipitation is seen to cause the normally monotonically decreasing electrical conductivity to actually increase above 900 K; the opposite trend is present in the Seebeck coefficient. The same carrier-concentration variation with temperature as was used for the bulk *n*-type case in Fig. 3 is also used here.
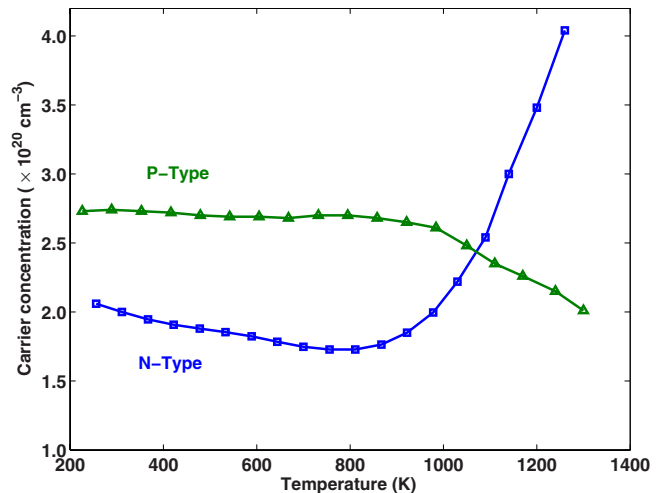

FIG. 8. (Color online) Extracted carrier concentration versus temperature for the *n*-type and *p*-type $Si_{0.8}Ge_{0.2}$ nanocomposites.
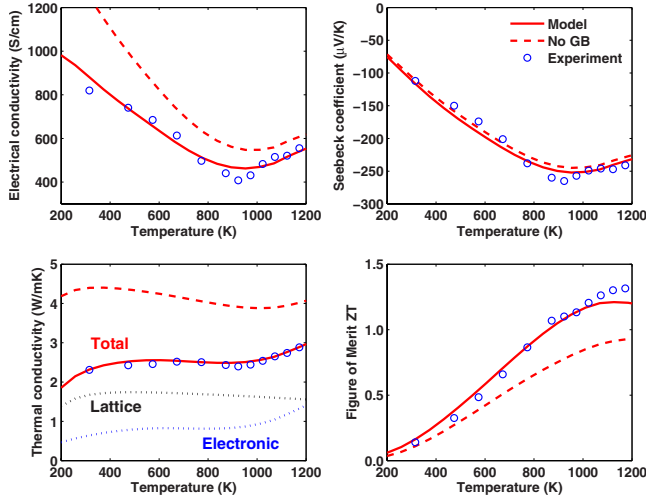
FIG. 9. (Color online) Calculated (curves) and experimental (symbols) thermoelectric properties for the n-type nanocomposite (data from Ref. 18). (Solid lines—model including GB scattering; dashed lines—model without GB scattering; dotted lines—electronic and lattice components of thermal conductivity.)

B. p type

Unfortunately, a completely consistent fit for the p-type nanocomposite could not be found. Specifically, the model is not able to predict the high Seebeck coefficient that is observed experimentally without adjustment to the hole effective mass. We find that increasing the hole effective mass from $1.2m_e$ to $1.55m_e$ is able to explain the data, possibly indicating the nanocomposite valence band is different from that of the bulk. A change in hole effective mass has been reported in strained $Si_{1-x}Ge_x/Si_{1-y}Ge_y$ thin films[62] but whether the same phenomenon is responsible for the observed nanocomposite properties is not clear.

The mobility is shown in Fig. 10. Unlike the n-type case, where ionized impurity scattering is dominant, here acoustic-
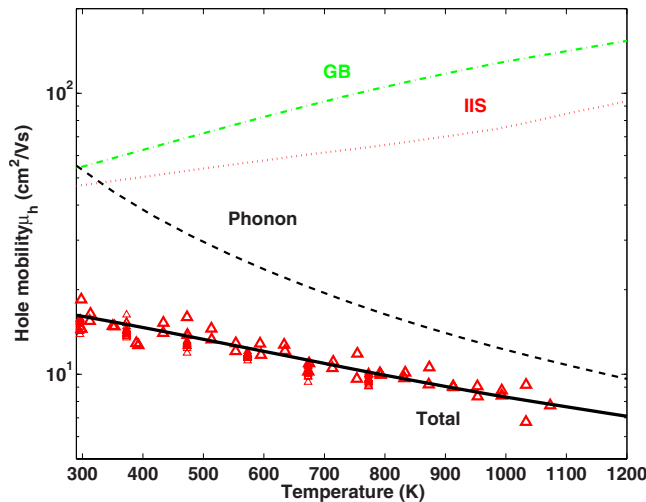

FIG. 10. (Color online) Calculated mobility for each scattering mechanism and total mobility (curves) with experimental data (symbols) for the p-type nanocomposite. (Solid line—total mobility; broken lines—mobility for each scattering mechanism.)
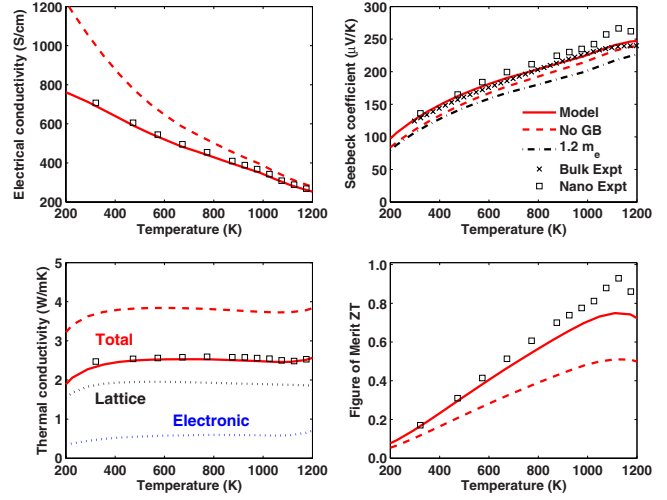

FIG. 11. (Color online) Calculated (curves) and experimental (symbols) thermoelectric properties for the p-type nanocomposite (data from Ref. 19) along with the bulk experimental data shown earlier for reference. (Solid lines—model including GB scattering; dashed lines—model without GB scattering; dotted lines—electronic and lattice components of thermal conductivity; dash-dotted line—Seebeck coefficient calculated using the bulk effective mass of $1.2m_e$.)

phonon scattering is the dominant scattering mechanism over most of the temperature range.

Figure 8 shows the hole concentration versus temperature. Unlike previous reports for bulk p-type $Si_{0.8}Ge_{0.2}$,[37] the nanocomposite does exhibit a change in hole concentration at elevated temperature, reducing from around 2.6×10^{20} cm^{-3} at room temperature to 2.0×10^{20} cm^{-3} at 1300 K. This is somewhat unexpected as carrier concentration changes in p-type $Si_{0.8}Ge_{0.2}$ had previously been observed only on the time scale of thousands of hours.[37] The explanation for this effect is similar to that for n-type dopant precipitation. At room temperature, the material is supersaturated with B but it must be raised to a higher temperature of about 1000 K to reject B from the lattice. The B rejection causes the hole concentration to reduce to a value closer to the solubility limit.

Figure 11 shows calculated thermoelectric properties for different conditions along with the experimental thermoelectric properties of the nanocomposite and bulk material. One set of curves is calculated using an effective mass of $1.55m_e$ and includes GB scattering while the second set does not include GB scattering but is otherwise the same. The Seebeck coefficient using the bulk effective mass of $1.2m_e$ has also been computed for comparison.

The calculated Seebeck coefficient obtained using the bulk effective mass of $1.2m_e$ is about 25% lower than the experimental data over the entire temperature range while that calculated using $1.55m_e$ gives a better fit. An interesting feature of the experimental data is that even though the hole concentration of the nanocomposite material is almost twice that of the bulk material (2.6×10^{20} cm^{-3} versus 1.35×10^{20} cm^{-3}), the Seebeck coefficient of the nanocomposite is actually equal to or higher than that of the bulk. We have tried many different types of GB scattering models, but none

predict the level of increase in Seebeck coefficient that is observed; only by increasing the effective mass are we able to obtain a satisfactory fit for all the properties. However, whether the material actually does have a different effective mass from the bulk is not clear, and more investigation into the transport properties and band structure of nanocomposite *p*-type $Si_{0.8}Ge_{0.2}$ is necessary.

VI. DISCUSSION

We used the model calculations to better understand the effects of GB scattering on the thermoelectric properties. To start, we examine the nanocomposite and bulk experimental data more closely. For both the *n*-type and *p*-type materials, the nanocomposite electrical conductivity is reduced from the calculated value without GB scattering at room temperature, but the difference decreases as the temperature increases. This is expected because the phonon-scattering rate goes as $T^{3/2}$ and thus becomes large compared to the other scattering mechanisms at high temperature, making the influence of GB scattering less significant as the temperature increases. Crucially, the phonon GB scattering rate is always much larger than the other phonon-scattering rates over the entire temperature range. Thus, while the nanocomposite electrical conductivity approaches that of the bulk at high temperature, the lattice thermal conductivity is still much lower than that of the bulk, leading to a net increase in *ZT* which is most pronounced at high temperature. Unfortunately, this also implies that improving the electrical properties at high temperature is difficult because the mobility is always limited by phonon scattering, especially in the *p*-type material.

The model can provide additional information about GB scattering. An interesting observation is that the GB potentials required to fit the data are several times higher than those predicted from the Poisson equation. Even with a very high trap density of $N_t = 1 \times 10^{13}$ cm^{-3} and a relatively lower doping concentration $N_D = 1 \times 10^{20}$ cm^{-3}, the magnitude of the GB potential is only predicted to be about 20 meV. However, the value required to fit the data is 45 meV. There could be several reasons for this. One likely possibility is that there are many more defects present than were accounted for in the model. TEM images show there are a variety of nanoprecipitates and composition variations that could also act as electron-scattering sites.[17–19] In the model only scattering sites from the nanoscale grain boundaries are taken into account but if the density of scattering sites is actually larger than this, the magnitude of the GB potential required to fit the data would decrease.

Another possibility is that nanocomposites have more disordered GB regions and thus more trapping states than have been previously measured for microcrystalline materials. The nanocomposite materials studied here are doped far beyond the solubility limit for the host material $Si_{0.8}Ge_{0.2}$ with the result that a large fraction of the inserted dopants are rejected from lattice sites and are forced into other regions of the material such as the GB. As an example, the *p*-type nanocomposite sample is doped with 5% B, or 2.5×10^{21} cm^{-3}, but the measured carrier concentration is only 2.6

$\times 10^{20}$ cm^{-3}, indicating that most of the dopants do not occupy substitutional sites in the lattice. It has been previously hypothesized that dopants might affect the number of trapping states in the GB, though if and to what extent the trapping states are modified is not known.[54] Unfortunately, it is not easy to determine the number of trapping states with common methods, such as capacitance measurements, due to the very small size of the grains.

Yet another possibility is that the grains are becoming so small that the volume fraction of GB is not negligible, making the material essentially composed of two phases, one being the host material and the inclusion phase being the GB material. Since the GB is expected to have very low mobility, the combined material's mobility will be lower than would be predicted from a scattering model alone.

While it is clear that many questions remain concerning transport in nanocomposites, the results discussed here do suggest several strategies and research topics which could lead to further improvements in *ZT*. One obvious topic for further research is determining how to fabricate nanocomposites with fewer defects and cleaner grain boundaries. If the number of defects or number of trapping states could be reduced, the GB scattering rate would be reduced and the mobility would increase, especially in the room temperature to intermediate temperature range. Understanding the reason for the mobility reduction and adjusting fabrication conditions to minimize it would thus be very helpful.

Another possible research topic is based on the observation that the lattice thermal conductivity has been reduced so far that it is nearing the electronic thermal conductivity; in the *n*-type case the electronic thermal conductivity is actually larger than the lattice component at high temperature. Unfortunately, this means that further reducing the lattice thermal conductivity will yield only marginal improvements in *ZT* as the lattice thermal conductivity approaches the electronic thermal conductivity. Research on ways to reduce the electronic and bipolar thermal conductivities such that *ZT* is increased would thus also be very useful.[63]

The final topic we discuss is the validity of the Boltzmann equation for highly doped thermoelectric materials. The Boltzmann equation is an equation for particle transport and neglects wave effects. For this approximation to be satisfied, it can be shown that the necessary condition is that the electron MFP be much longer than the wavelength.[25] However, as shown in Fig. 5, for highly doped $Si_{0.8}Ge_{0.2}$ the electron MFP is predicted to be even shorter than its wavelength, making the applicability of the Boltzmann equation somewhat questionable. The prediction of the wavelength being longer than the mean-free path may also be caused by the inaccuracy of scattering models, which are mostly derived assuming that the doping level is not too high. Thermoelectric materials are very highly doped and are usually degenerate, however, and their electrical properties are sometimes closer to those of metals than to semiconductors. Thus while the Boltzmann equation has been successful in explaining most of the experimental data, a predictive capability for the transport properties of nanocomposites will require a more powerful formalism.

VII. CONCLUSION

In this paper we have used the Boltzmann equation under the relaxation-time approximation to calculate the thermoelectric properties of nanocomposite $Si_{1-x}Ge_x$ alloys. The strong grain-boundary scattering mechanism in nanocomposites is accounted for using phonon and electron grain-boundary scattering models. We find that the calculations are in excellent agreement with the reported properties for the *n*-type nanocomposite but the experimental Seebeck coefficient for the *p*-type nanocomposite is larger than the model's prediction. Increasing the hole effective mass gives a better fit, possibly indicating the valence band in the nanocomposite is different from that of the bulk material. We also find that dopant precipitation is an important process in both *n*-type and *p*-type nanocomposites, in contrast to bulk SiGe, where dopant precipitation is most significant only in *n*-type

materials. Finally, the model shows that the grain-boundary potential required to fit the data is several times larger than the value obtained using the Poisson equation. This suggests that an improvement in electrical properties is possible by reducing the number of defects in the grain or reducing the number of electrical trapping states at the grain boundaries.

*gchen2@mit.edu

†daryoosh.vashaee@okstate.edu

[1] L. D. Hicks and M. S. Dresselhaus, Phys. Rev. B **47**, 16631 (1993).

[2] G. Chen, *Recent Trends in Thermoelectric Materials Research III*, Semiconductors and Semimetals Vol. 71 (Academic, New York, 2001), pp. 203–259.

[3] R. Venkatasubramanian, *Recent Trends in Thermoelectric Materials Research III*, Semiconductors and Semimetals Vol. 71 (Academic, New York, 2001), pp. 175–201.

[4] R. Venkatasubramanian, E. Siivola, T. Colpitts, and B. O'Quinn, Nature (London) **413**, 597 (2001).

[5] T. C. Harman, P. J. Taylor, M. P. Walsh, and B. E. LaForge, Science **297**, 2229 (2002).

[6] G. Chen and A. Shakouri, J. Heat Transfer **124**, 242 (2002).

[7] K. F. Hsu, S. Loo, F. Guo, W. Chen, J. S. Dyck, C. Uher, T. Hogan, E. K. Polychroniadis, and M. G. Kanatzidis, Science **303**, 818 (2004).

[8] P. F. P. Poudeu, J. D'Angelo, A. D. Downey, J. L. Short, T. P. Hogan, and M. G. Kanatzidis, Angew. Chem., Int. Ed. **45**, 3835 (2006).

[9] P. C. Zhai, W. Y. Zhao, Y. Li, L. S. Liu, X. F. Tang, Q. J. Zhang, and M. Niino, Appl. Phys. Lett. **89**, 052111 (2006).

[10] J. R. Sootsman, R. J. Pcionek, H. Kong, C. Uher, and M. G. Kanatzidis, Chem. Mater. **18**, 4993 (2006).

[11] M. Dresselhaus, G. Chen, M. Y. Tang, R. G. Yang, H. Lee, D. Z. Wang, Z. F. Ren, J. P. Fleurial, and P. Gogna, Adv. Mater. (Weinheim, Ger.) **19**, 1043 (2007).

[12] J. Androulakis, C. H. Lin, H. J. Kong, C. Uher, C. I. Wu, T. Hogan, B. A. Cook, T. Caillat, K. M. Paraskevopoulos, and M. G. Kanatzidis, J. Am. Chem. Soc. **129**, 9780 (2007).

[13] G. J. Snyder and E. S. Toberer, Nature Mater. **7**, 105 (2008).

[14] A. I. Hochbaum, R. Chen, R. D. Delgado, W. Liang, E. C. Garnett, M. Najarian, A. Majumdar, and P. Yang, Nature (London) **451**, 163 (2008).

[15] A. I. Boukai, Y. Bunimovich, J. Tahir-Kheli, J.-K. Yu, W. A. Goddard III, and J. R. Heath, Nature (London) **451**, 168 (2008).

[16] B. Poudel, Q. Hao, Y. Ma, Y. Lan, A. Minnich, B. Yu, X. Yan, D. Wang, A. Muto, D. Vashaee, X. Chen, J. Liu, M. S. Dresselhaus, G. Chen, and Z. F. Ren, Science **320**, 634 (2008).

[17] Y. Ma, Q. Hao, B. Poudel, Y. Lan, B. Yu, D. Wang, G. Chen, and Z. F. Ren, Nano Lett. **8**, 2580 (2008).

[18] X. W. Wang, H. Lee, Y. C. Lan, G. H. Zhu, G. Joshi, D. Z. Wang, J. Yang, A. J. Muto, M. Y. Tang, J. Klatsky, S. Song, M. S. Dresselhaus, G. Chen, and Z. F. Ren, Appl. Phys. Lett. **93**, 193121 (2008).

[19] G. Joshi, H. Lee, Y. Lan, X. Wang, G. Zhu, D. Wang, R. W. Gould, D. C. Cuff, M. Y. Tang, M. S. Dresselhaus, G. Chen, and Z. F. Ren, Nano Lett. **8**, 4670 (2008).

[20] G. S. Nolas, J. Sharp, and H. Goldsmid, *Thermoelectrics: Basic Principles and New Materials Developments* (Springer, New York, 2001).

[21] *Thermoelectrics Handbook: Macro to Nano*, edited by D. Rowe (CRC, Boca Raton, 2006).

[22] R. Yang, G. Chen, and M. Dresselhaus, Nano Lett. **5**, 1111 (2005).

[23] R. Yang, G. Chen, and M. S. Dresselhaus, Phys. Rev. B **72**, 125418 (2005).

[24] G. Chen, *Nanoscale Energy Transport and Conversion* (Oxford University Press, New York, 2005).

[25] M. Lundstrom, *Fundamentals of Carrier Transport*, 2nd ed. (Cambridge University Press, Cambridge, 2000).

[26] J. Singh, *Physics of Semiconductors and their Heterostructures* (McGraw-Hill, Singapore, 1996).

[27] B. R. Nag, *Electron Transport in Compound Semiconductors*, Springer Series in Solid-State Sciences Vol. 11 (Springer, New York, 1980).

[28] C. B. Vining, J. Appl. Phys. **69**, 331 (1991).

[29] G. A. Slack and M. A. Hussain, J. Appl. Phys. **70**, 2694 (1991).

[30] A. F. Mayadas and M. Shatzkes, Phys. Rev. B **1**, 1382 (1970).

[31] M. M. Mandurah, K. C. Saraswat, and T. I. Kamins, IEEE Trans. Electron Devices **28**, 1163 (1981).

[32] D. P. Joshi and R. S. Srivastava, IEEE Trans. Electron Devices **31**, 920 (1984).

[33] M. K. Sharma and D. P. Joshi, J. Appl. Phys. **102**, 033704 (2007).

[34] D. Vashaee and A. Shakouri, J. Appl. Phys. **95**, 1233 (2004).

[35] B. M. Askerov, *Electron Transport Phenomena in Semiconductors* (World Scientific, Singapore, 1994).

[36] Yu. I. Ravich, B. A. Efimova, and V. I. Tamarchenko, Phys. Status Solidi B **43**, 11 (1971).

[37] V. S. Shukla and D. M. Rowe, Phys. Status Solidi A **66**, 243 (1981).

[38] D. M. Rowe and N. Savvides, J. Phys. D **12**, 1613 (1979).

[39] N. Savvides and D. M. Rowe, J. Phys. D **14**, 723 (1981).

[40] Y. I. Ravich, B. A. Efimova, and I. A. Smirnov, *Semiconducting Lead Chalcogenides*, Monographs in Semiconductor Physics Vol. 5 (Plenum, New York, 1970).

[41] D. L. Rode, Phys. Rev. B **2**, 1012 (1970).

[42] A. Schenk, *Advanced Physical Models for Silicon Device Simulation, Computational Microelectronics* (Springer, New York, 1998).

[43] D. K. Ferry, *Semiconductors* (Macmillan, New York, 1991).

[44] B. Ridley, *Quantum processes in semiconductors* (Oxford University Press, New York, 1999).

[45] R. Brunetti, C. Jacoboni, F. Nava, L. Reggiani, G. Bosman, and R. J. J. Zijlstra, J. Appl. Phys. **52**, 6713 (1981).

[46] C. Jacoboni and L. Reggiani, Rev. Mod. Phys. **55**, 645 (1983).

[47] E. F. Steigmeier and B. Abeles, Phys. Rev. **136**, A1149 (1964).

[48] M. V. Fischetti and S. E. Laux, Phys. Rev. B **48**, 2244 (1993).

[49] http://www.ioffe.rssi.ru/SVA/NSM/Semicond/index.html. Accessed April 2008.

[50] J. Callaway, Phys. Rev. **113**, 1046 (1959).

[51] J. P. Dismukes, L. Ekstrom, E. F. Steigmeier, I. Kudman, and D. S. Beers, J. Appl. Phys. **35**, 2899 (1964).

[52] T. I. Kamins, J. Appl. Phys. **42**, 4357 (1971).

[53] J. Y. W. Seto, J. Appl. Phys. **46**, 5247 (1975).

[54] C. R. M. Grovenor, J. Phys. C **18**, 4079 (1985).

[55] M. S. Dresselhaus, G. Chen, Z. F. Ren, J.-P. Fleurial, P. Gogna, M. Y. Tang, D. Vashaee, H. Lee, X. Wang, G. Joshi, G. Zhu, D. Wang, R. Blair, S. Bux, R. Kaner, *Nanocomposites to Enhance ZT in Thermoelectrics*, Proceedings of the MRS Fall Meeting 2007, p. 1044–U02–04.

[56] M.-S. Jeng, R. Yang, D. Song, and G. Chen, J. Heat Transfer **130**, 042410 (2008).

[57] R. Prasher, J. Appl. Phys. **100**, 034307 (2006).

[58] R. Prasher, J. Appl. Phys. **100**, 064302 (2006).

[59] W. Kim, J. Zide, A. Gossard, D. Klenov, S. Stemmer, A. Shakouri, and A. Majumdar, Phys. Rev. Lett. **96**, 045901 (2006).

[60] A. Khitun, K. L. Wang, and G. Chen, Nanotechnology **11**, 327 (2000).

[61] A. Minnich and G. Chen, Appl. Phys. Lett. **91**, 073105 (2007).

[62] S. Chun and K. Wang, IEEE Trans. Electron Devices **39**, 2153 (1992).

[63] A. J. Minnich, M. S. Dresselhaus, Z. F. Ren, and G. Chen, Energy Environ. Sci. **2**, 466 (2009).

[64] V. Palankovski, Ph.D. thesis, Technical University of Wien, 2000.